



Supplement of

Measurement report: The importance of biomass burning in light extinction and direct radiative effect of urban aerosol during the COVID-19 lockdown in Xi'an, China

Jie Tian et al.

Correspondence to: Qiyuan Wang (wangqy@ieecas.cn) and Junji Cao (jjcao@mail.iap.ac.cn)

The copyright of individual parts of the supplement might differ from the article licence.

16 **Text S1.** Absorption Ångström exponent method

17 In this study, aerosol light absorption coefficient (b_{abs}) values at wavelengths of $\lambda = 370$ nm, 470 nm,
18 520 nm, 590 nm, 660 nm, and 880 nm were measured by a newly developed Aethalometer (Model
19 AE33, Magee Scientific, Berkeley, CA, USA). The Absorption Ångström exponent (AAE) describes
20 the wavelength dependence of aerosol light absorption and can be calculated according to power law
21 fitting b_{abs} at wavelengths of 370 nm to 880 nm (Moosmüller et al., 2011) as below:

22
$$b_{\text{abs}}(\lambda) \sim \lambda^{-\text{AAE}} \quad (1)$$

23 Through the AAE method (Lack and Langridge, 2013), the mass absorption efficiency (MAE) of black
24 carbon (BC) at 520 nm (in $\text{m}^2 \text{g}^{-1}$) can be obtained as follows:

25
$$b_{\text{abs}}(520 \text{ nm}) = b_{\text{abs-BC}}(520 \text{ nm}) + b_{\text{abs-BrC}}(520 \text{ nm}) \quad (2)$$

26
$$b_{\text{abs-BC}}(520 \text{ nm}) = b_{\text{abs-BC}}(880 \text{ nm}) \times \left(\frac{520}{880}\right)^{-\text{AAE}_{\text{BC}}} \quad (3)$$

27
$$\text{MAE}_{\text{BC}}(520 \text{ nm}) = \frac{b_{\text{abs-BC}}(520 \text{ nm})}{[\text{BC}]} \quad (4)$$

28 Here, $b_{\text{abs-BC}}$ and $b_{\text{abs-BrC}}$ (in Mm^{-1}) are the light absorption coefficients caused by BC and brown
29 carbon (BrC) respectively; AAE_{BC} is the AAE caused by the BC particle, which can vary from 0.8 to
30 1.4 due to core size, coating materials, and mixing state (Lack and Cappa, 2010; Lack and Langridge,
31 2013). The linear relationship between the AAEs and the mass concentration ratios of organic aerosol
32 (OA) to BC is investigated to find the realistic AAE_{BC} during the normal and lockdown periods (Fig.
33 S12) (Yuan et al., 2016); and $[\text{BC}]$ is the mass concentration of BC (in $\mu\text{g m}^{-3}$).

44 **Text S2.** Uncertainty of the element concentration

45 Considering the element concentration measured by the Xact 625i ambient metals monitor with a 1-
46 hour sampling interval, the uncertainty of the element concentration (u_e) inputting into the receptor
47 model was estimated as follows (Norris et al., 2014):

48
$$u_e = \sqrt{(c_e \times 10 \%)^2 + (0.5 \times \text{MDL})^2}, \text{ for } c_e > \text{MDL} \quad (5)$$

49
$$u_e = \frac{5}{6} \times \text{MDL}, \text{ for } c_e \leq \text{MDL} \quad (6)$$

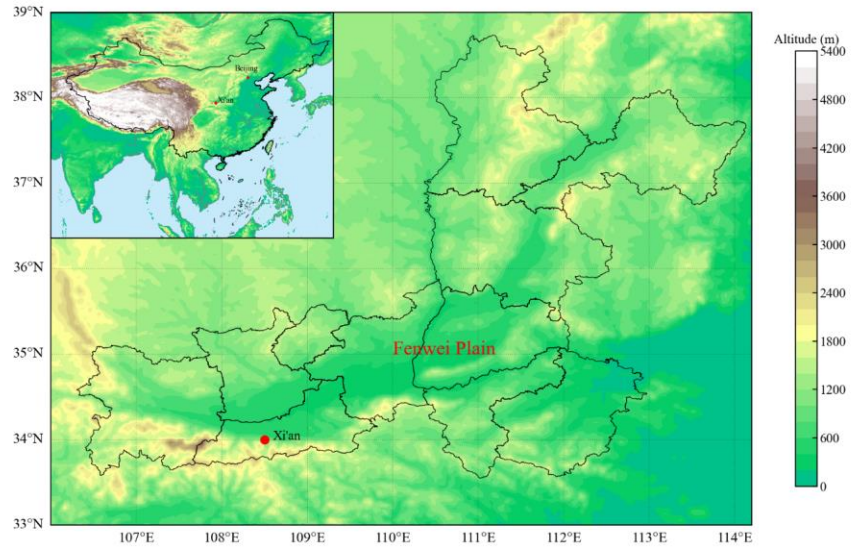
50 Here, c_e is the concentration of the element; 10 % is the default analytical relative error (Rai et al., 2020);
51 and MDL represents the method detection limit of the element.

52 **Text S3.** Diagnostics of HERM solutions

53 In this study, factor numbers from two to eight were selected to run in the HERM software. Each factor
54 solution was performed with completely unconstrained profiles at twenty different seeds to explore the
55 possible sources. Detailed information on how the most interpretable factors were selected is presented
56 below.

57 As shown in Fig. S3, the values of $Q/Q_{\text{exp}} (> 1)$ decreased as the factor numbers increased. The large
58 Q/Q_{exp} values in two- (21.10 ± 0.03) and three-factor (12.29 ± 0.01) solutions indicated too few factors
59 were resolved. In the four-factor solution (Fig. S4), Factor 2 identified as biomass burning was
60 characterized by high explained variations (EV) values of POA (56 %), LO-OOA (54 %), BC (43 %),
61 Cl (55 %). Factor 3 was regarded as fugitive dust due to significant EV values of Si (100 %), Ca (68 %),
62 and Fe (35 %). For the Factor 4 assigned to the secondary source, EV values of NO_3^- , SO_4^{2-} , NH_4^+ , and
63 MO-OOA were larger than 30 %. It is noted that Factor 1 was associated with the traffic-like source
64 because b_{ext} from this source showed a moderate correlation with NO_x , a tracer of fresh motor vehicle
65 exhaust emission ($R^2 = 0.58$). However, the high EV values of some specific elements (e.g. As (44 %)
66 and Se (31 %)) in this factor indicated the possible mixture of other fossil fuel sources (e.g. coal
67 combustion). When five factors were resolved, except traffic-like source (Factor 1), biomass burning
68 (Factor 2), and fugitive dust (Factor 3), the secondary source was split into the nitrate and SOA (Factor
69 4) and the sulfate and SOA (Factor 5) sources (Fig. S5). The increase to six-factor solution (Fig. S6)
70 showed well separation of traffic-related emissions (Factor 1) and coal combustion (Factor 3). A
71 stronger correlation between b_{ext} from traffic-related emissions and NO_x ($R^2 = 0.72$) was found
72 compared to traffic-like factors resolved in four- and five- factor solutions ($R^2 = 0.58$). As shown in
73 Figs. S7 and S8, further investigations of unconstrained profile solutions with seven and eight factors
74 resulted in factor split. The extra split factors possibly came from biomass burning and coal combustion,
75 mainly due to high EV values of K (26 %–33 %) and As (21 %). Despite b_{ext} from coal combustion
76 factors in seven- and eight- factor solutions showed the stronger correlation with As ($R^2 = 0.63$ – 0.68),
77 Se ($R^2 = 0.79$ – 0.86), and Pb ($R^2 = 0.60$ – 0.67), the profiles identified coal combustion had no POA
78 contribution. Meanwhile, the values of POA in fugitive dust profiles identified in seven- and eight-
79 factor solutions were higher than 1 (the reference standard of $\text{PM}_{2.5}$). It is indicated that these profiles
80 did not match the real world.

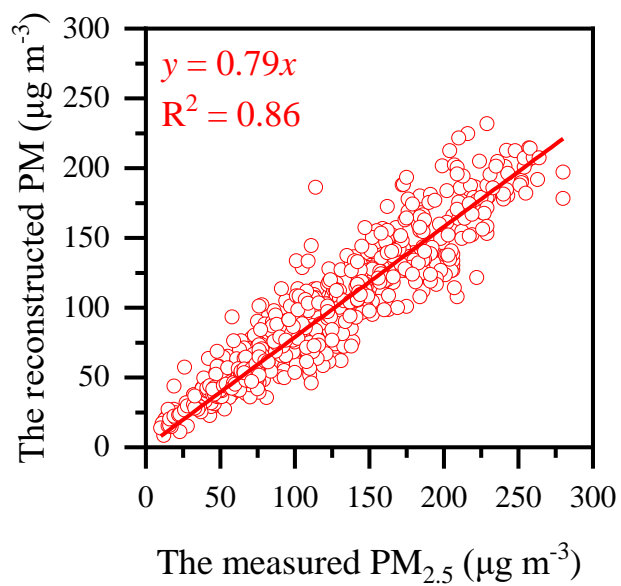
81 Therefore, as the factor solutions described above, six factors were the most interpretable in our study,
82 including traffic-related emissions, biomass burning, coal combustion, fugitive dust, the nitrate and
83 SOA source, and the sulfate and SOA source.



84

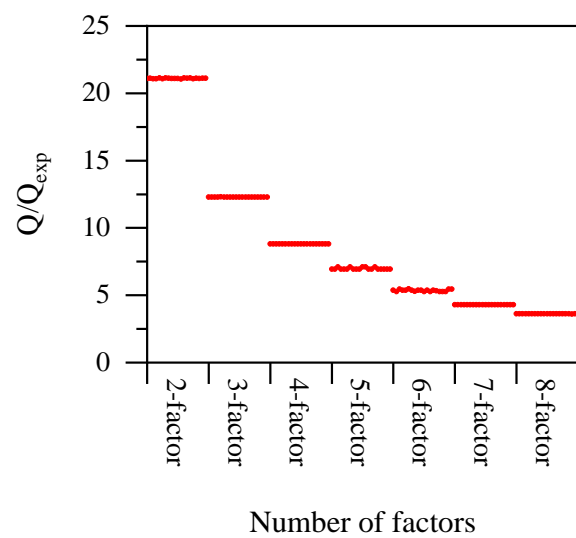
85

Figure S1. The location of the sampling site in Xi'an, China.



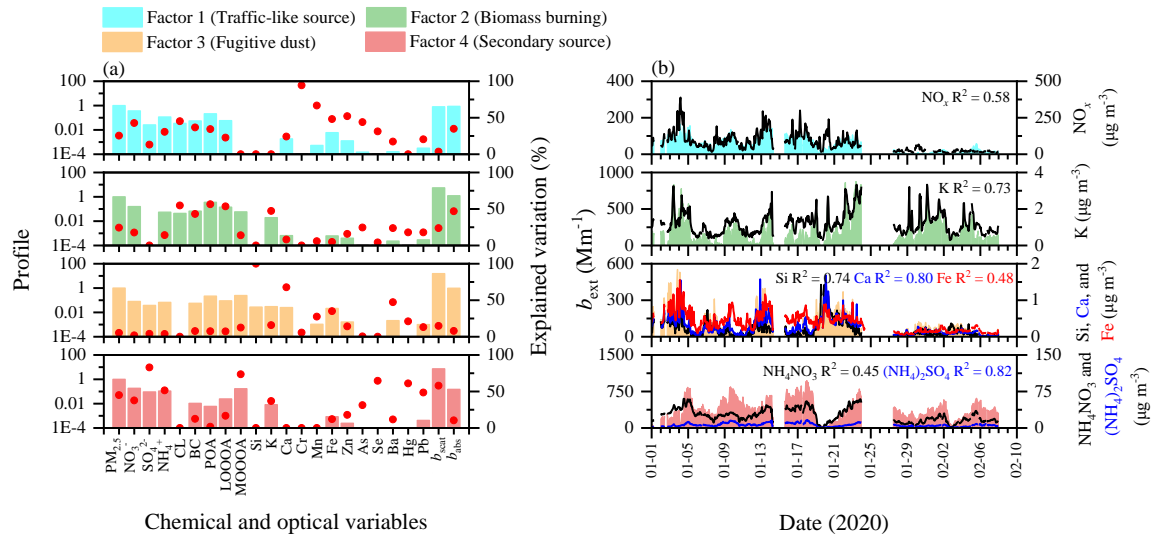
86

87 **Figure S2.** Linear relationship between the measured PM_{2.5} concentration and the sum concentration of
88 POA, LO-OOA, MO-OOA, NH₄NO₃, (NH₄)₂SO₄, BC, and fine soil (the sum is referred to as the
89 reconstructed PM).



90

91 **Figure S3.** Values of Q/Q_{exp} for the unconstrained profile solutions with two to eight factors at twenty
92 different seeds.

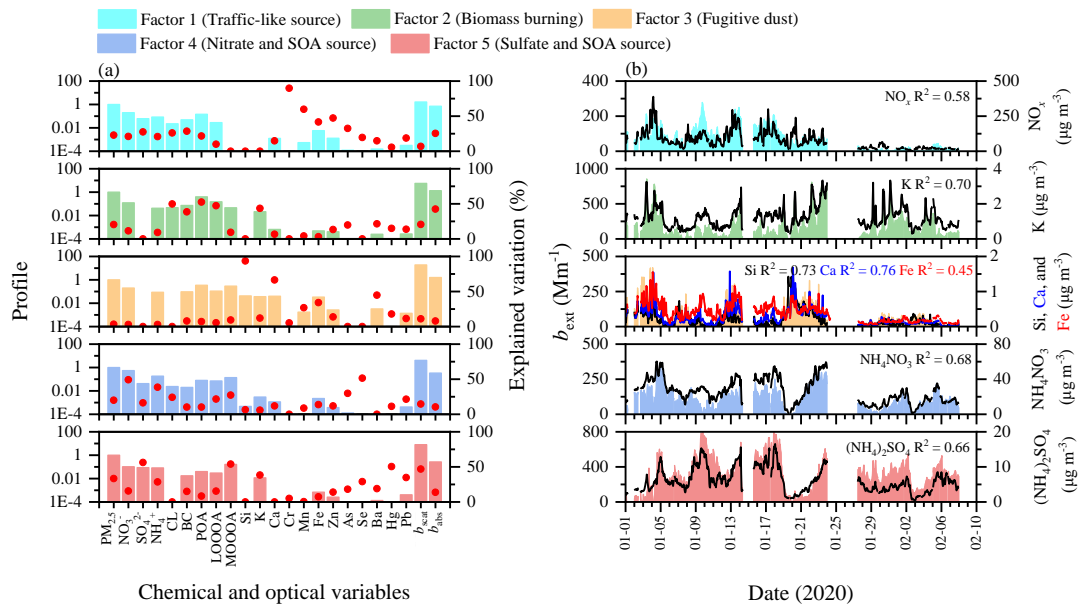


93

Chemical and optical variables

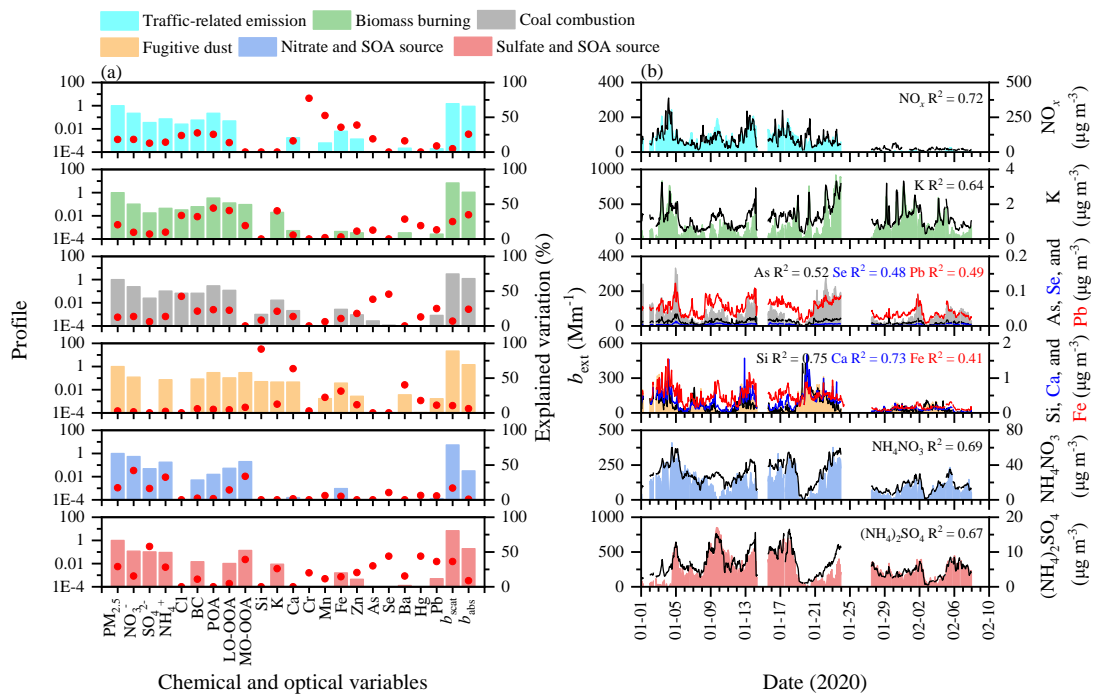
Date (2020)

94 **Figure S4.** (a) Profiles and (b) time series plots of the resolved source factors in the four-factor solution.
 95 The columns in each factor are the profile that displays the relative relation of the absolute values of
 96 variables. The red dot represents the explained variation in species for different factors. The
 97 corresponding time trends of chemical tracers also are shown.



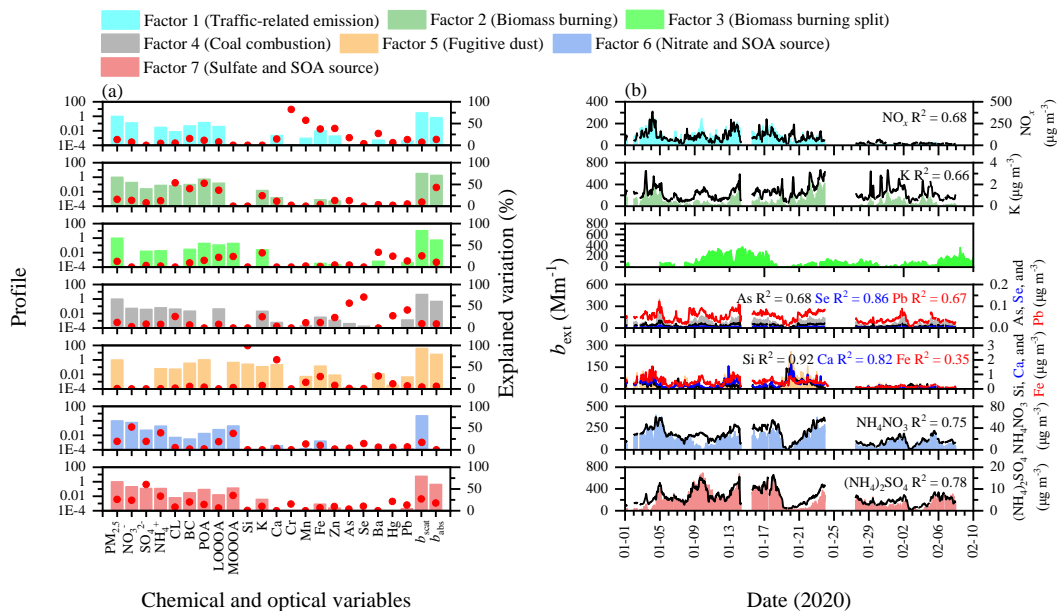
98

99 **Figure S5.** (a) Profiles and (b) time series plots of the resolved source factors in the five-factor solution.
 100 The columns in each factor are the profile that displays the relative relation of the absolute values of
 101 variables. The red dot represents the explained variation in species for different factors. The
 102 corresponding time trends of chemical tracers also are shown.



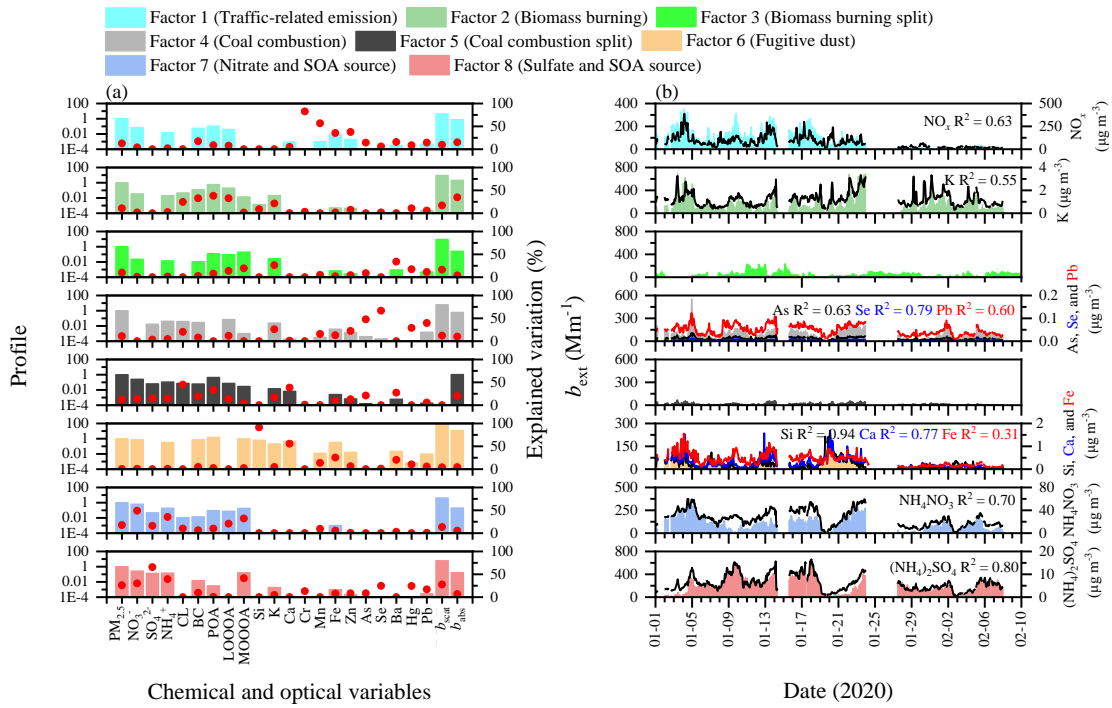
103

104 **Figure S6.** (a) Profiles and (b) time series plots of the resolved source factors in the six-factor solution.
 105 The columns in each factor are the profile that displays the relative relation of the absolute values of
 106 variables. The red dot represents the explained variation in species for different factors. The
 107 corresponding time trends of chemical tracers also are shown.



108

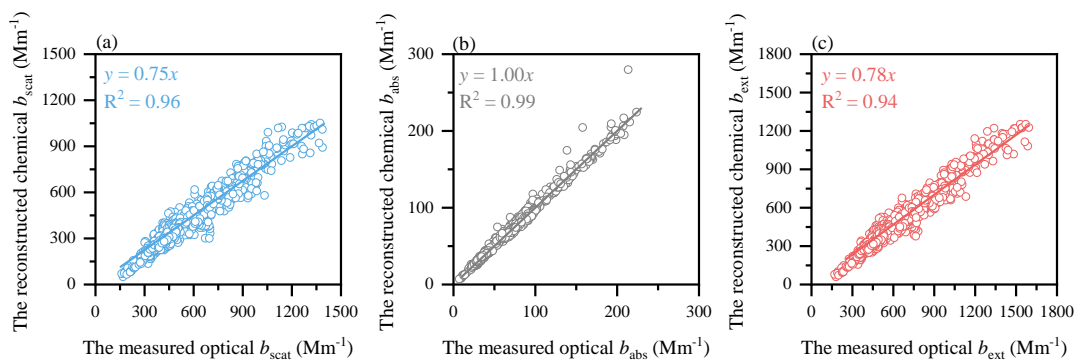
109 **Figure S7.** (a) Profiles and (b) time series plots of the resolved source factors in the seven-factor solution.
 110 The columns in each factor are the profile that displays the relative relation of the absolute values of
 111 variables. The red dot represents the explained variation in species for different factors. The
 112 corresponding time trends of chemical tracers also are shown.



113

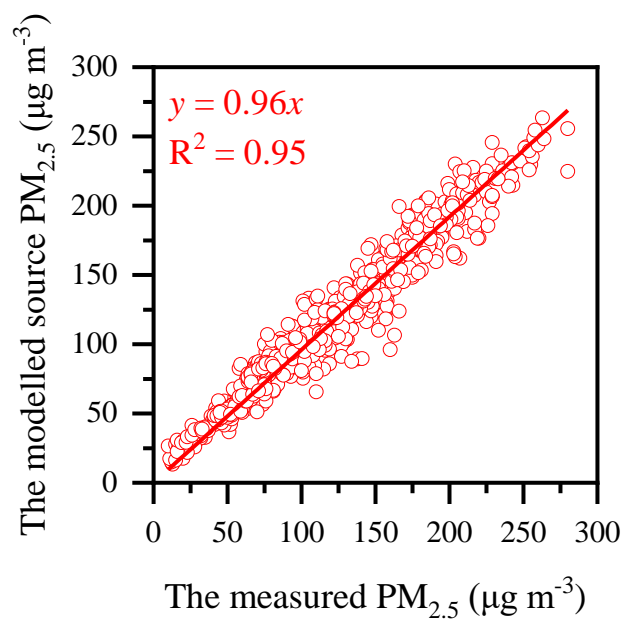
114 **Figure S8.** (a) Profiles and (b) time series plots of the resolved source factors in the eight-factor solution.

115 The columns in each factor are the profile that displays the relative relation of the absolute values of
 116 variables. The red dot represents the explained variation in species for different factors. The
 117 corresponding time trends of chemical tracers also are shown.



118

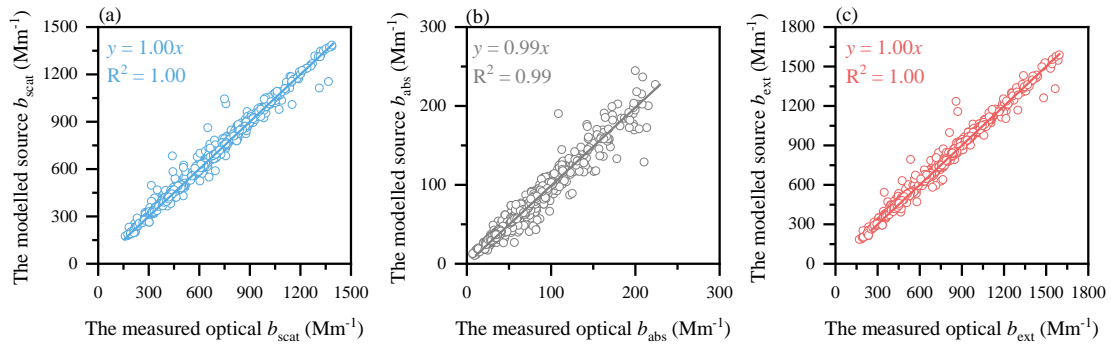
119 **Figure S9.** Linear relationships between the reconstructed chemical and the measured optical (a) b_{scat} ,
 120 (b) b_{abs} , and (c) b_{ext} .



121

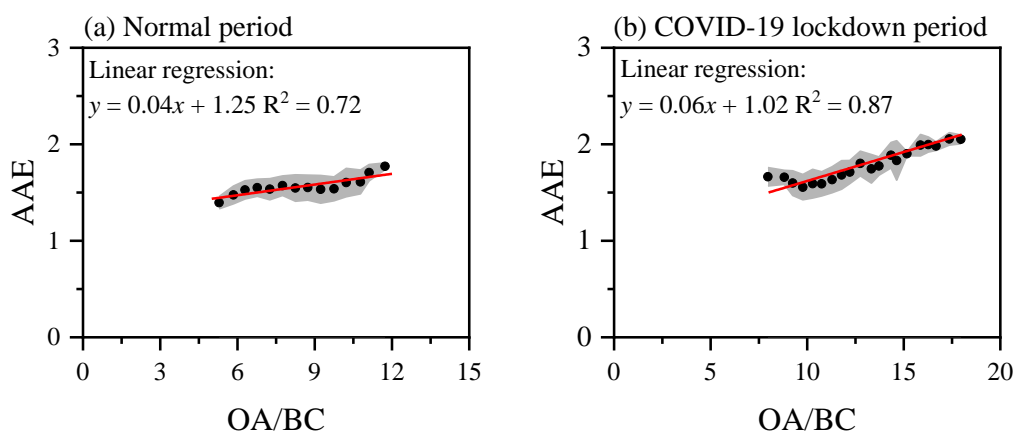
122 **Figure S10.** Linear relationship between the modelled source and the measured PM_{2.5} mass
123 concentrations. The modelled source PM_{2.5} was strongly correlated linearly with the measured PM_{2.5}
124 ($R^2 = 0.95$, slope = 0.96), indicating that the six identified sources can adequately account for the
125 variability in PM_{2.5} mass concentration.

126



127

128 **Figure S11.** Linear relationships between the modelled source and the measured optical (a) b_{scat} , (b) b_{abs} ,
 129 and (c) b_{ext} . The modelled source b_{scat} , b_{abs} , and b_{ext} were strongly correlated linearly with the measured
 130 optical b_{scat} ($R^2 = 1.00$, slope = 1.00), b_{abs} ($R^2 = 0.99$, slope = 0.99), and b_{ext} ($R^2 = 1.00$, slope = 1.00),
 131 indicating that the six identified sources can adequately account for the variability in aerosol optical
 132 coefficients.



133

134 **Figure S12.** Linear relationships between the AAEs and the mass concentration ratios of organic aerosol
 135 (OA) to BC (OA/BC) during the normal (a) and lockdown (b) periods. The intercept of the linear
 136 regression represents the realistic AAE_{BC} . The points and light gray shadows represent the mean values
 137 and error margins in each bin ($\Delta(OA/BC) = 0.5$).

138 **Table S1.** Summary of chemical and meteorological measurements of in Xi'an before and during the
 139 COVID-19 lockdown period.

Parameters	Sampling interval	Instruments and online source	Operation and calibration
Chemical variables			
NO ₃ ⁻ , SO ₄ ²⁻ , NH ₄ ⁺ , Cl ⁻ , and OA	15-min	Quadrupole aerosol chemical speciation monitor (Q-ACSM, Aerodyne Research Inc., Billerica, Massachusetts, USA)	The relative ionization efficiencies (RIEs) for OA, nitrate, and chloride were set to 1.4, 1.1, and 1.3 by default respectively. The RIE for ammonium (5.8) was determined from the ammonium nitrate aerosol calibration, while the RIE for sulfate (1.9) was estimated by fitting the measured sulfate versus predicted sulfate values. The collection efficiency was set to 0.45.
Si, K, Ca, Cr, Mn, Fe, Zn, As, Se, Ba, Hg, and Pb	1-hour	Xact 625i ambient metals monitor (Xact 625i, Cooper Environmental Services, Beaverton, OR, USA)	Daily advanced quality assurance checks were performed during 30 min after midnight to monitor shifts in the calibration.
PM _{2.5} and NO _x	5-min	The Department of Ecology and Environment of Shaanxi Province (http://sthjt.shaanxi.gov.cn , in Chinese)	
Meteorological variables*			
WS, WD, T, P, and DP	1-hour	Integrated automatic weather station (MAWS201, Vaisala, Helsinki, Finland)	
PBLH	3-hour	Global Data Assimilation System (ftp://arlftp.arlhq.noaa.gov/pub/archives/gdas1)	PBLH at the sampling site was obtained using linear interpolation method.

140 *WS, WD, T, P, DP, and PBLH represent wind speed, wind direction, temperature, pressure, dew point,
 141 and planetary boundary layer height respectively.

142 **Table S2.** Summary of output indices from the constructed b_{ext} GAM.

Intercept	6.64	
Adjusted R ²	0.54	
Smoothed parameters*	F value	<i>p</i> value
$f(\text{WS})$	3.402	0.002331
$f(\text{WD})$	5.820	0.000134
$f(\text{T})$	2.707	0.012809
$f(\text{P})$	3.209	0.001757
$f(\text{DP})$	13.325	$< 2.00 \times 10^{-16}$
$f(\text{PBLH})$	3.656	0.026822

143 *WS, WD, T, P, DP, and PBLH represent wind speed, wind direction, temperature, pressure, dew point,
 144 and planetary boundary layer height respectively.

145 **Table S3.** Concurvity indices between each independent smoothed parameter in the constructed GAM.

Smoothed parameters*	$f(\text{WS})$	$f(\text{WD})$	$f(\text{T})$	$f(\text{P})$	$f(\text{DP})$	$f(\text{PBLH})$
$f(\text{WS})$	1.00	0.28	0.03	0.09	0.07	0.23
$f(\text{WD})$	0.15	1.00	0.08	0.09	0.03	0.07
$f(\text{T})$	0.06	0.07	1.00	0.11	0.25	0.22
$f(\text{P})$	0.08	0.24	0.08	1.00	0.06	0.09
$f(\text{DP})$	0.05	0.06	0.08	0.07	1.00	0.05
$f(\text{PBLH})$	0.13	0.07	0.05	0.04	0.06	1.00

146 *WS, WD, T, P, DP, and PBLH represent wind speed, wind direction, temperature, pressure, dew point,
 147 and planetary boundary layer height respectively.

148 **References**

- 149 Lack, D. A. and Cappa, C. D.: Impact of brown and clear carbon on light absorption enhancement,
150 single scatter albedo and absorption wavelength dependence of black carbon, *Atmos. Chem.*
151 *Phys.*, 10, 4207–4220, <https://doi.org/10.5194/acp-10-4207-2010>, 2010.
- 152 Lack, D. A. and Langridge, J. M.: On the attribution of black and brown carbon light absorption
153 using the Ångström exponent, *Atmos. Chem. Phys.*, 13, 10535–10543,
154 <https://doi.org/10.5194/acp-13-10535-2013>, 2013.
- 155 Moosmüller, H., Chakrabarty, R. K., Ehlers, K. M., and Arnott, W. P.: Absorption Ångström
156 coefficient, brown carbon, and aerosols: basic concepts, bulk matter, and spherical particles,
157 *Atmos. Chem. Phys.*, 11, 1217–1225, <https://doi.org/10.5194/acp-11-1217-2011>, 2011.
- 158 Norris, G., Duvall, R., Brown, S., and Bai, S.: EPA positive matrix factorization (PMF) 5.0
159 fundamentals and user guide, U.S. Environmental Protection Agency, Washington, DC,
160 EPA/600/R-14/108 (NTIS PB 2015-105147),
161 https://cfpub.epa.gov/si/si_public_record_report.cfm?Lab=NERL&direntryid=308292, 2014.
- 162 Rai, P., Furger, M., Slowik, J. G., Canonaco, F., Fröhlich, R., Hüglin, C., Minguillón, M. C., Petterson,
163 K., Baltensperger, U., and Prévôt, A. S. H.: Source apportionment of highly time-resolved elements
164 during a firework episode from a rural freeway site in Switzerland, *Atmos. Chem. Phys.*, 20, 1657–
165 1674, <https://doi.org/10.5194/acp-20-1657-2020>, 2020.
- 166 Yuan, J. F., Huang, X. F., Cao, L. M., Cui, J., Zhu, Q., Huang, C. N., Lan, Z. J., and He, L. Y.:
167 Light absorption of brown carbon aerosol in the PRD region of China, *Atmos. Chem. Phys.*,
168 16, 1433–1443, <https://doi.org/10.5194/acp-16-1433-2016>, 2016.